Anomalous lattice thermal conductivity in SrLiX (X = P, As) Zintl phases via anion engineering

Yanchun Xu(徐艳春), Ning Wang(王宁), Hui Zhang(张慧), Shuli Li(李淑丽), Zhiping Fang(方治平), Yijing Wang(王艺憬), Yanhui Liu(刘艳辉), Tian Cui(崔田)

Citation: Chin. Phys. B. 35, 106102 (2026). DOI: 10.1088/1674-1056/ae9075 | CSTR: 32038.14.CPB.ae9075
http://cpb.iphy.ac.cn; http://iopscience.iop.org/cpb

What follows is a list of articles you may be interested in

High-pressure synthesis, crystal structure, and electronic properties of $Ba_9Zr_{2.79}Te_{15}$

Runteng Chen(陈润滕), Guodong Wang(王国东), Zhe Wang(王哲), Wenmin Li(李文敏), Jianfa Zhao(赵建发), Zheng Deng(邓正), Heng Wang(王恒), Xiancheng Wang(望贤成), Jun Zhang(张俊), Changqing Jin(靳常青)
Chin. Phys. B. 35, 066101 (2026). DOI: 10.1088/1674-1056/ae521a | CSTR: 32038.14.CPB.ae521a

Electronic and thermal properties of Ag-doped single crystal zinc oxide via laser-induced technique

Huan Xing(邢欢), Hui-Qiong Wang(王惠琼), Tinglu Song(宋廷鲁), Chunli Li(李纯莉), Yang Dai(戴扬), Gengming Fu(傅耿明), Junyong Kang(康俊勇), Jin-Cheng Zheng(郑金成)
Chin. Phys. B. 32, 066107 (2023). DOI: 10.1088/1674-1056/acae74

Pressure-induced stable structures and physical properties of Sr–Ge system

Shuai Han(韩帅), Shuai Duan(段帅), Yun-Xian Liu(刘云仙), Chao Wang(王超), Xin Chen(陈欣), Hai-Rui Sun(孙海瑞), Xiao-Bing Liu(刘晓兵)
Chin. Phys. B. 32, 016101 (2023). DOI: 10.1088/1674-1056/ac6db5

Theoretical study on electronic structure and thermoelectric properties of PbS_xTe_{1-x} (x=0.25, 0.5, and 0.75) solid solution

Yong Lu(鲁勇), Kai-yue Li(李开跃), Xiao-lin Zhang(张晓林), Yan Huang(黄艳), Xiao-hong Shao(邵晓红)
Chin. Phys. B. 27, 026103 (2018). DOI: 10.1088/1674-1056/27/2/026103

Electronic and thermoelectric properties of $Mg_2Ge_xSn_{1-x}$ (x=0.25, 0.50, 0.75) solid solutions by first-principles calculations

Kai-yue Li(李开跃), Yong Lu(鲁勇), Yan Huang(黄艳), Xiao-hong Shao(邵晓红)
Chin. Phys. B. 26, 066103 (2017). DOI: 10.1088/1674-1056/26/6/066103

SPECIAL TOPIC — A 40th Anniversary Celebration: Physics Research and Innovation at Ningbo University

Anomalous lattice thermal conductivity in SrLiX (X = P, As) Zintl phases via anion engineering

Yanchun Xu(徐艳春)[1], Ning Wang(王宁)[1], Hui Zhang(张慧)[1], Shuli Li(李淑丽)[1], Zhiping Fang(方治平)[1], Yijing Wang(王艺憬)[2], Yanhui Liu(刘艳辉)[1,†], and Tian Cui(崔田)[1,3,‡]

[1] *Institute of High-Pressure Physics and School of Physical Science and Technology, Ningbo University, Ningbo* 315211, *China*
[2] *WLSA Shanghai Academy, Shanghai* 200940, *China*
[3] *State Key Laboratory of High Pressure and Superhard Materials, College of Physics, Jilin University, Changchun* 130012, *China*

(Received 28 May 2026; revised manuscript received 14 July 2026; accepted manuscript online 27 July 2026)

Thermoelectric materials show promise for converting waste heat into electricity, addressing energy sustainability challenges. The ZrBeSi-type Zintl phase compounds, featuring a layered structure, intrinsically exhibit low lattice thermal conductivity (κ_L). Motivated by this feature, we employed first-principles calculations combined with Boltzmann transport theory to systematically investigate the thermoelectric transport properties of SrLiX (X = P, As). SrLiP exhibits a κ_L of 0.98 W·m^{-1}·K^{-1} at 900 K, which is 34% lower than that of SrLiAs (1.48 W·m^{-1}·K^{-1}), despite its smaller average atomic mass. This anomalous reduction originates from the broader phonon bandwidth in SrLiP, which is a direct consequence of anion regulation, and this broader bandwidth substantially expands the three-phonon scattering phase space and enhances phonon scattering rates. Meanwhile, n-type SrLiAs and SrLiP reach power factors of 1.14 mW · m^{-1} · K^{-2} and 1.33 mW · m^{-1} · K^{-2} at 900 K, respectively, benefiting from multiple band convergence near the Fermi level that yields a valley degeneracy. Ultimately, our calculations yield ZT values of 0.73 for n-type SrLiP and 0.48 for n-type SrLiAs at 900 K. Our results demonstrate that anion engineering successfully decouples thermal and electrical transport, simultaneously suppressing lattice thermal conductivity while maintaining favorable electrical transport properties. This offers a viable strategy for designing high-performance thermoelectrics.

Keywords: Zintl phase compounds, thermoelectric performance, lattice thermal conductivity, anion engineering

PACS: 61.66.–f, 72.15.Jf

DOI: 10.1088/1674-1056/ae9075 **CSTR:** 32038.14.CPB.ae9075

1. Introduction

Thermoelectric materials can convert heat into electricity, offering a promising route for waste heat recovery in the face of the intensifying energy crisis.[1–4] Energy conversion efficiency is characterized by the dimensionless thermoelectric figure of merit $ZT = S^2\sigma T/(\kappa_e + \kappa_L)$, where S, σ, κ_e, and κ_L denote the Seebeck coefficient, electrical conductivity, electronic thermal conductivity, and lattice thermal conductivity, respectively.[5–8] In general, S, σ, and κ_L are typically difficult to tune independently, and this strong coupling between electrical and thermal transport limits improvements in the ZT value.[9,10] Therefore, identifying new material systems that simultaneously possess high electrical transport performance and low κ_L is of great significance for thermoelectric materials research. Recent studies have demonstrated that Heusler compounds,[11–13] perovskite-type complex oxides,[14,15] chalcogenides,[16,17] and Zintl-phase compounds are promising candidates for thermoelectric applications.[18–22]

In particular, Zintl-phase compounds[18–22] show significant promise for improving the thermoelectric figure of merit, owing to their characteristic "phonon-glass, electron-crystal" (PGEC) nature.[23–27] This unique behavior originates from their structural characteristics: the rigid covalent framework provides efficient pathways for electron transport, ensuring high electrical conductivity, while the loosely bound cations significantly reduce the lattice thermal conductivity, giving rise to intrinsically low κ_L in this class of materials.[20,28] Among various Zintl-phase families, compounds with two-dimensional covalent-bonded substructures have received particular attention due to their favorable electrical transport properties.[29] The ZrBeSi-type Zintl phase compounds, a representative example of such systems, feature a layered anionic network that is favorable for electron transport. This layered structure allows for variation in the anionic species, which has been found to effectively modulate κ_L and decouple thermal and electrical transport.[30] ACuSb (A = Ca, Sr, Ba)[31] and KBaBi[32] have been demonstrated to achieve high n-type ZT values of approximately 2.2 at 700 K and 3 at 1000 K, respec-

†Corresponding author. E-mail: liuyanhui@nbu.edu.cn
‡Corresponding author. E-mail: cuitian@nbu.edu.cn

© 2026 Chinese Physical Society and IOP Publishing Ltd. All rights, including for text and data mining, AI training, and similar technologies, are reserved.

tively, benefiting from their layered architecture.

In this work, we systematically investigate the thermoelectric transport properties of SrLiX (X = P, As) using first-principles calculations combined with Boltzmann transport theory. According to the classical Slack model, lattice thermal conductivity decreases with increasing average atomic mass.[33] Surprisingly, our calculations show the opposite trend: the compound containing the lighter P exhibits an anomalously lower κ_L compared to the one with the heavier As. At 900 K, the lattice thermal conductivity of SrLiP is 0.98 W·m^{-1}·K^{-1}, whereas that of SrLiAs under the same temperature is 1.48 W·m^{-1}·K^{-1}. This unexpected behavior originates from the larger phonon bandwidth in SrLiP, which enhances phonon scattering and ultimately results in lower lattice thermal conductivity while maintaining favorable electrical transport properties, indicating that anion engineering effectively decouples electronic and thermal transport in this Zintl-phase system. Ultimately, we found that at 900 K, the ZT values of SrLiAs and SrLiP reach 0.48 and 0.73, respectively. Our work expands the understanding of ZrBeSi-type Zintl phases and provides a new strategy for designing high-performance thermoelectric materials through anion engineering.

2. Methodology

First-principles calculations were performed using the projector augmented wave (PAW) method within density functional theory (DFT), as implemented in Vienna *ab initio* simulation package (VASP).[34,35] All calculations were performed using a plane-wave cutoff energy of 500 eV. A $12\times12\times6$ k-point mesh generated using the Monkhorst–Pack scheme was employed for Brillouin zone sampling. To account for exchange-correlation effects, the generalized gradient approximation (GGA) with the Perdew–Burke–Ernzerhof (PBE) parametrization was utilized.[36] The electronic self-consistent field convergence criterion was set to 10^{-8} eV, and the crystal structures were fully relaxed until the Hellmann–Feynman forces acting on each atom were less than 10^{-4} eV·Å^{-1}. The PBE functional is known to severely underestimate the band gap of semiconductors. To address this issue, we used the HSE06 hybrid functional to determine the band gap and electronic band structure of SrLiX (X = P, As).[37]

We carried out phonon calculations on the relaxed crystal structures using the Phonopy software package.[38] A $3\times3\times2$ supercell was employed, together with a $4\times4\times3$ k-point grid, to obtain the second-order harmonic interatomic force constants (IFCs) and phonon dispersion relations. Anharmonic interactions must be considered to calculate the relaxation time τ. Accordingly, we employed the Thirdorder package with the same supercell geometry to obtain third-order IFCs, which are necessary for describing three-phonon scattering processes.[39] Interactions up to the ninth nearest neighboring atoms were considered. The lattice thermal conductivity was then calculated by iteratively solving the Peierls–Boltzmann transport equation for phonons using the ShengBTE code.[40] The κ_L tensor is given by

$$\kappa_L^{\alpha\beta}(T)=\frac{1}{N\Omega}\sum_{\lambda}C_{\lambda}(T)v_{\lambda}^{\alpha}v_{\lambda}^{\beta}\tau_{\lambda}(T), \tag{1}$$

where N denotes the total number of q-points, Ω is the volume of the unit cell, α and β indicate the Cartesian components, λ represents the phonon mode index, C_{λ} stands for the mode-resolved specific heat capacity, v_{λ}^{α} and v_{λ}^{β} are the group velocity components, and τ_{λ} corresponds to the phonon lifetime.

For electronic transport properties, the band structure was first calculated using the hybrid HSE06 functional to obtain accurate band gaps, as mentioned above. Subsequently, the electrical transport coefficients were evaluated using the AMSET code, which solves the Boltzmann transport equation within the relaxation time approximation.[41,42] The scattering rate for an electron from the initial state $n\boldsymbol{k}$ to the final state $\boldsymbol{k}+\boldsymbol{q}$ is described by

$$\tau^{-1}_{n\boldsymbol{k}\to m\boldsymbol{k}+\boldsymbol{q}}=\frac{2\pi}{\hbar}|g_{nm}(\boldsymbol{k},\boldsymbol{q})|^2\delta(\varepsilon_{n\boldsymbol{k}}-\varepsilon_{m\boldsymbol{k}+\boldsymbol{q}}). \tag{2}$$

Here, $\hbar$ denotes the reduced Planck constant, δ is the Dirac delta function, ε represents the electron energy, and g stands for the coupling matrix element. Multiple scattering mechanisms were taken into account, including acoustic deformation potential (ADP) scattering, polar optical phonon (POP) scattering, and ionized impurity (IMP) scattering.[43–45] The total scattering rate was obtained by summing the individual contributions following Matthiessen's rule:

$$\frac{1}{\tau}=\frac{1}{\tau_{\mathrm{ADP}}}+\frac{1}{\tau_{\mathrm{IMP}}}+\frac{1}{\tau_{\mathrm{POP}}}. \tag{3}$$

3. Results and discussion

3.1. Crystal structure and stability

Zintl-phase compounds SrLiX (X = P, As) crystallize in the $P6_3/mmc$ space group, and their crystal structures along with the electron localization function (ELF) are shown in Fig. 1(a). Along the crystallographic c axis, the Li–X layers and Sr atomic layers are arranged alternately. The atomic arrangement in this system is well ordered, exhibiting good periodicity and structural regularity. The ELF indicates that the Li–X bonds exhibit a polar covalent character biased toward the X atom, whereas the interaction between Li and Sr is predominantly ionic. For a more comprehensive analysis of the structural features, the negative crystal orbital Hamilton population (–COHP) values were computed, as presented in Fig. 1(b). The –COHP values further reveal that the Li–X bonds possess stronger bond strength than the Li–Sr bonds. This difference in bond strength contributes to the formation

of a layered crystal structure, which is beneficial for impeding thermal transport.

The thermodynamic stability of the investigated materials was evaluated at 300 K, 600 K, and 900 K via *ab initio* molecular dynamics (AIMD) simulations, using the same $3 \times 3 \times 2$ supercell as employed in the phonon calculations. The results for SrLiP and SrLiAs are presented in Figs. 1(c) and S10, respectively. The free energy remains stable throughout the 15 ps simulation, with negligible fluctuations confined to a narrow range, demonstrating the thermodynamic stability of the system. In addition, mechanical stability was assessed by calculating the elastic constants, which measure the resistance of the crystal to structural deformation under external stress, with the detailed values summarized in Table S1 in the supplementary material. According to the Born mechanical stability criteria,[46,47] for the hexagonal crystal structure, the elastic constants must satisfy the following conditions:

$$C_{11} > |C_{12}|, \quad C_{33}(C_{11}+C_{12}) > 2C_{13}^2, \quad C_{44} > 0. \tag{4}$$

The calculated results satisfy the stability criteria, confirming the mechanical stability of the material.

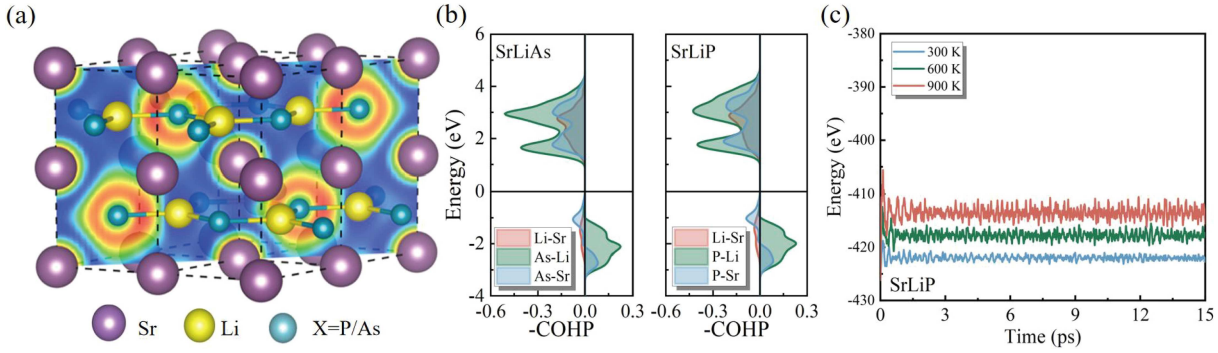

Fig. 1. (a) Lattice structure and calculated electron localization function (ELF) on the (110) plane. The purple, yellow, and blue spheres represent Sr, Li, and *X* (P or As) atoms, respectively. (b) Negative crystal orbital Hamilton population (–COHP) analysis for SrLiAs and SrLiP. (c) Free energy as a function of time for SrLiP at 300 K, 600 K, and 900 K over 15 ps.

3.2. Thermal transport

As presented in Fig. S1, our calculations show that within the SrLiX (X = P, As) system, κ_L exhibits a T^{-1} temperature dependence. Moreover, both compounds exhibit anisotropic κ_L, as detailed in Fig. S6. For both compounds, the lattice thermal conductivity along the a-axis is lower than that along the c-axis. Generally, κ_L decreases with increasing average atomic mass in crystalline compounds.[48] However, our calculations show that SrLiP has a lower κ_L than SrLiAs, which contradicts this general trend. This observation indicates that the average atomic mass is not the dominant factor governing the lattice thermal conductivity in the SrLiX system.

To explain the thermal transport properties of SrLiX, we examined the phonon dispersion and phonon density of states (pDOS) of both SrLiAs and SrLiP, as illustrated in Figs. 2(a) and 2(b), respectively. The pDOS analysis reveals that the acoustic phonon modes originate mainly from the vibrations of the heavier Sr atoms, while the lighter X and Li atoms mainly contribute to the optical phonon modes. Notably, SrLiP exhibits a broader phonon bandwidth, reaching 205 cm^{-1} as indicated by the shaded region in Fig. 2(b), whereas SrLiAs shows a much narrower bandwidth of only 126 cm^{-1} (Fig. 2(a)). The expansion of the phonon bandwidth increases the phase space for phonon–phonon scattering, which increases the number of scattering channels and ultimately enhances the scattering rates, thereby contributing to the reduction of κ_L.

We further analyzed the frequency-dependent contributions to κ_L and the cumulative κ_L as a function of frequency at different temperatures for both compounds, as illustrated in Figs. 2(c) and 2(d), respectively. The analysis reveals that optical phonons make a substantial contribution to the lattice thermal conductivity of SrLiX. Interestingly, in comparison with SrLiAs, the contribution from optical phonons in the range of 40–100 cm^{-1} is substantially more suppressed in SrLiP. This suppression aligns with the region where the phonon bandwidth is enlarged (Fig. 2(b)), indicating that the broader bandwidth is responsible for this phenomenon. Therefore, the reduction in κ_L observed in SrLiP relative to SrLiAs likely originates from this pronounced suppression in the differential phonon spectrum.

The empirical formula for lattice thermal conductivity is given by $\kappa_L = \frac{1}{3}\sum_\lambda C_\lambda v_\lambda^2 \tau_\lambda$, where C_λ is the phonon-specific heat, v_λ is the group velocity, and τ_λ is the phonon lifetime. We systematically compared the phonon group velocities of both compounds within these frequency ranges in Fig. S5. SrLiP exhibits higher phonon group velocities. The phonon lifetime τ_λ is inversely proportional to the phonon scattering rate ($\tau_\lambda \propto 1/\Gamma_\lambda$).[49,50] Therefore, we calculated the phonon scattering rates of SrLiP and SrLiAs at 300 K, 600 K, and 900 K to investigate the κ_L behavior of these materials, as depicted in Figs. 3(a) and 3(b). With increasing temperature, more phonons are excited, leading to enhanced scatter-

ing rates. In the mid-frequency region associated with optical phonon modes (140 cm^{-1}), notably, SrLiP exhibits a pronounced scattering peak across all temperatures, and the intensity of this peak increases with rising temperature. This peak leads to a reduction in κ_L.

To understand the origin of this scattering peak, we first examined the three-phonon scattering phase space for both compounds, as shown in Figs. 3(c) and 3(d). Correspondingly, the phase space analysis reveals that a distinct peak structure exists in the same frequency region, as indicated by the shaded area in Fig. 3(d), which corresponds exactly to the observed scattering peak in SrLiP. As previously shown in the phonon

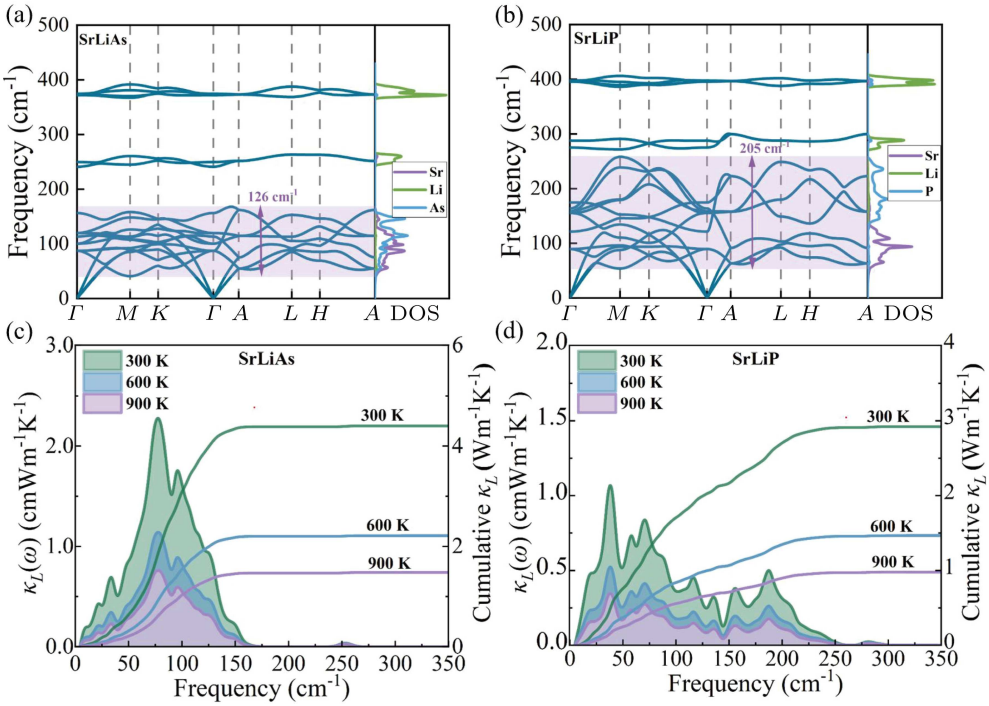

Fig. 2. Calculated phonon dispersion and phonon density of states for (a) SrLiAs and (b) SrLiP. Frequency-dependent cumulative and derivative κ_L for (c) SrLiAs and (d) SrLiP at 300 K, 600 K, and 900 K.

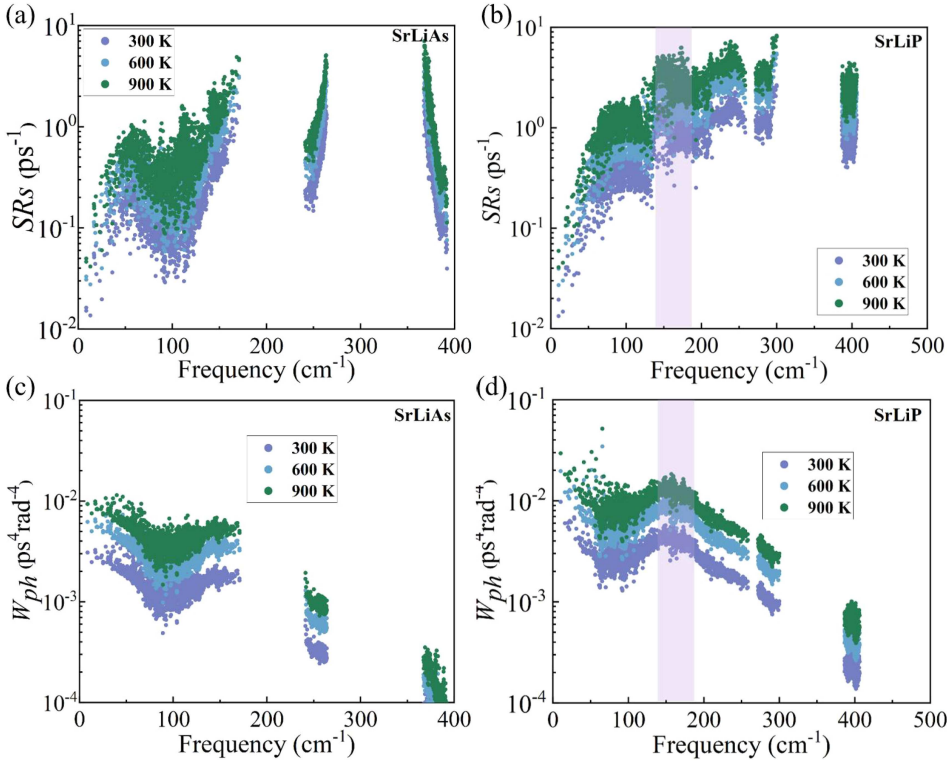

Fig. 3. The three-phonon scattering rates for (a) SrLiAs and (b) SrLiP at 300 K, 600 K, and 900 K. The calculated scattering phase space at 300 K, 600 K, and 900 K for (c) SrLiAs and (d) SrLiP.

dispersion relations in Fig. 2(b), the enhanced phase space features arise from the broader phonon bandwidth in SrLiP, which offers more scattering channels. The phonon scattering rate is jointly governed by the scattering phase space and material anharmonicity.[51,52] Then, we took into account the anharmonicity of both materials and presented their mode-resolved Grüneisen parameters projected onto the phonon branches in Fig. S2. For SrLiP, the Grüneisen parameters exhibit a marked increase around 140 cm^{-1}, indicating enhanced anharmonicity in this frequency range. Therefore, the scattering peaks observed in the shaded regions arise from the synergistic effects of both the scattering phase space and the anharmonicity of the materials. The emergence of these scattering peaks significantly reduces the phonon lifetime in SrLiP, leading to a more pronounced suppression in the dominant κ_L contribution region compared to SrLiAs. This result explains the anomalous dependence of κ_L on atomic mass in SrLiP.

3.3. Electron transport properties

Electrical transport properties are essential to thermoelectric performance. Therefore, we calculated the electronic band structures and density of states (DOS) of SrLiAs and SrLiP, as presented in Figs. 4(a) and 4(b). Both compounds exhibit indirect band gaps. Specifically, the band gap increases as the atomic mass of the anion X decreases, from 1.91 eV in SrLiAs to 2.08 eV in SrLiP. As revealed by the DOS analysis, near the Fermi level, the valence band maximum (VBM) of SrLiX (X = P, As) arises primarily from the X atoms, whereas the conduction band minimum (CBM) is mainly derived from the Sr atoms. The enlargement of the band gap in SrLiX results from the synergistic effects of anion size and electronegativity. Smaller anions restrict atomic orbital overlap, while their higher electronegativity enhances level splitting, which collectively broadens the band gap.[53]

The remarkable electronic transport properties of SrLiX stem from the coexistence of light and heavy bands. This unique band structure, combined with a high electronic band degeneracy, synergistically enhances the electrical transport performance.[54–56] As summarized in Table S2 of the supplementary material, taking SrLiP as an example, the electron effective masses are $0.110m_0$ (Γ–A) and $0.773m_0$ (Γ–K), and the hole effective masses are $2.962m_0$ (M–Γ) and $0.256m_0$ (M–K). These large variations across different crystallographic directions reflect significant anisotropy in carrier effective masses. Additionally, the presence of both a small electron effective mass and a large hole effective mass along M–Γ in SrLiP points to the coexistence of light and heavy bands. The light bands, characterized by their high carrier mobility, markedly improve electrical conductivity, whereas the heavy bands, with their larger effective mass, enhance the Seebeck coefficient.[57] These unique band structures are conducive to a high power factor.

Figure 5 presents the carrier concentration dependence of the Seebeck coefficient and electrical conductivity for both n-type and p-type SrLiX (X = P, As). The Seebeck coefficient increases gradually with increasing temperature from 300 K to 900 K. As the carrier concentration decreases, the Seebeck coefficient increases. In contrast, the electrical conductivity, as depicted in Figs. 5(c) and 5(d), exhibits the opposite trend: it decreases gradually with increasing temperature from 300 K to 900 K, while increasing with higher carrier concentration. Notably, both the Seebeck coefficient and the electrical conductivity of the n-type materials are higher than those of their p-type counterparts across the investigated temperature and carrier concentration ranges. This observation can be attributed to the higher band degeneracy at the CBM, which is consistent with the band structure analysis discussed above.

Building on the analysis of S and σ, we evaluated PF for both n-type and p-type SrLiX (X = P, As), as depicted in Fig. 6. For n-type SrLiX, the PF increases substantially with temperature and shows a non-monotonic dependence on carrier concentration, first increasing to a maximum and then decreasing. Notably, n-type SrLiX exhibits a higher PF, with SrLiP reaching a value of 1.33 $mW \cdot m^{-1} \cdot K^{-2}$ at 900 K and SrLiAs reaching 1.14 $mW \cdot m^{-1} \cdot K^{-2}$ at 900 K. This can be attributed to the favorable combination of band features at the CBM of SrLiX. The CBM of SrLiX possesses multiple valley degeneracy and the coexistence of light and heavy bands.

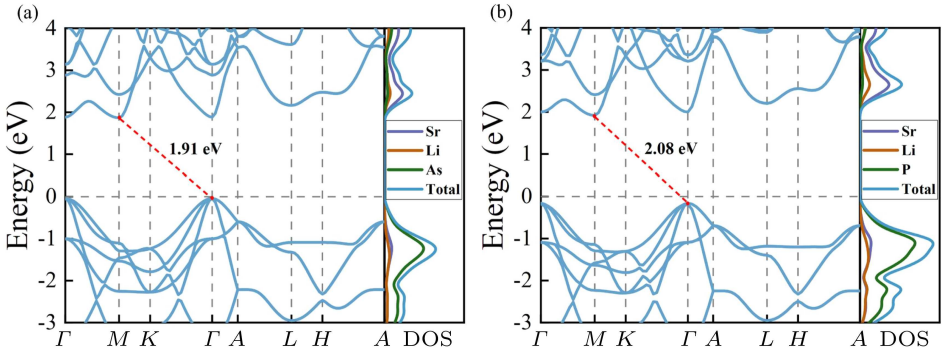

Fig. 4. The electronic band structures and density of states (DOS) of (a) SrLiAs and (b) SrLiP. The conduction band minimum (CBM) and valence band maximum (VBM) are located at the M and K points, respectively. The red dashed arrows indicate the bandgap values of 1.91 eV for SrLiAs and 2.08 eV for SrLiP.

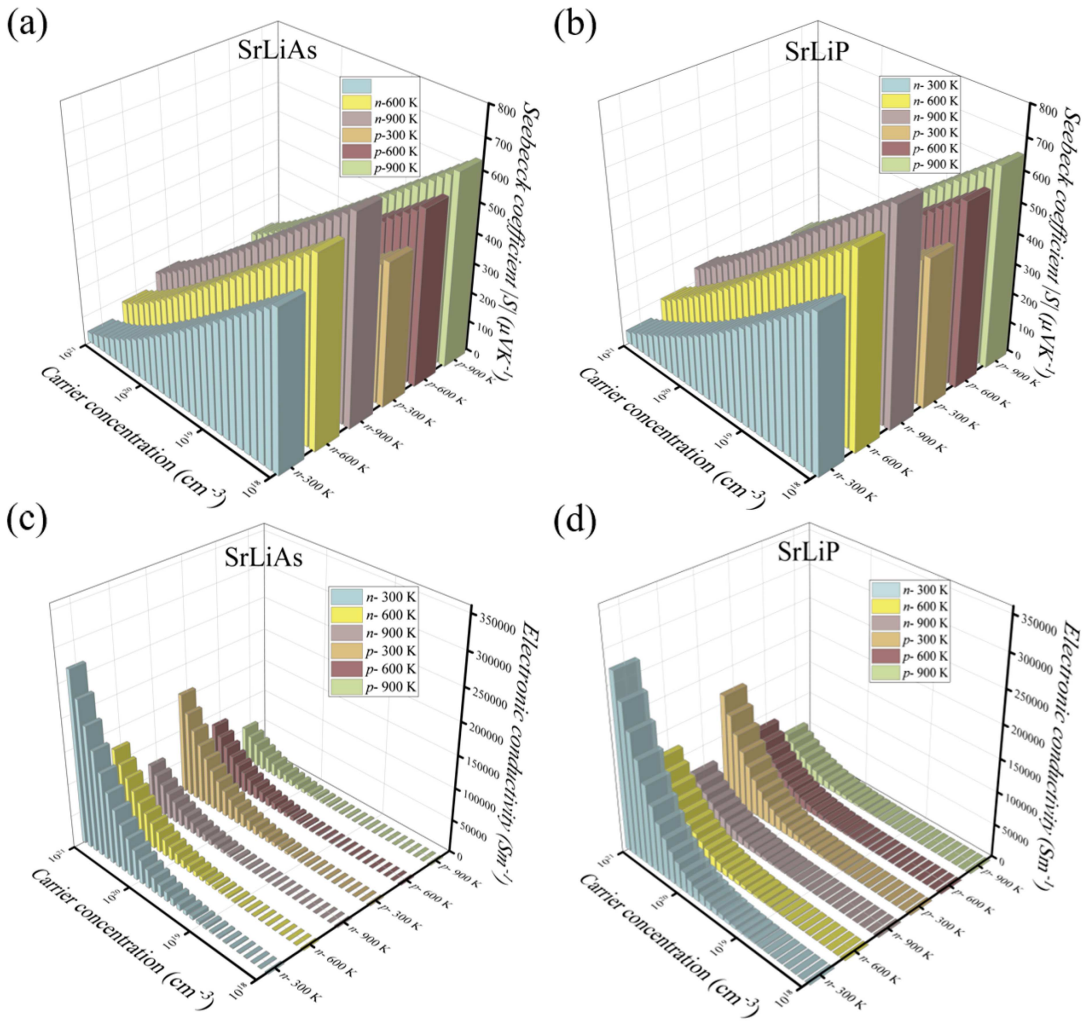

Fig. 5. The absolute value of S and the calculated σ of SrLiAs and SrLiP as a function of carrier concentration at 300 K, 600 K, and 900 K.

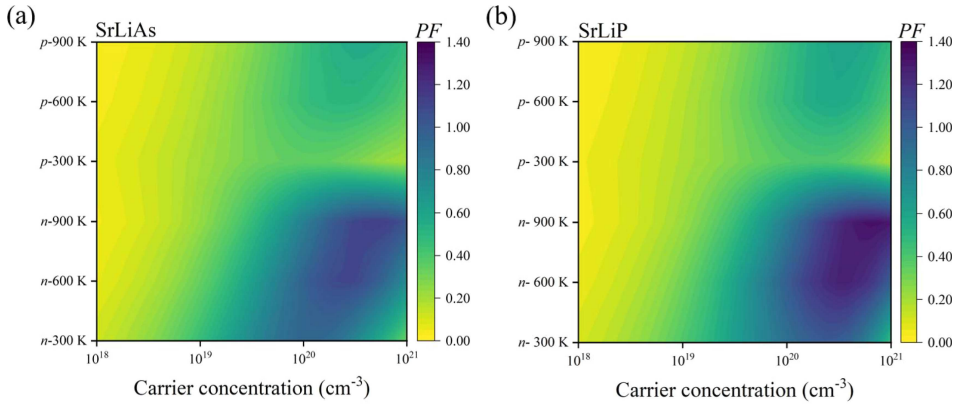

Fig. 6. The calculated PF of n-type and p-type SrLiAs and SrLiP as a function of carrier concentration at 300 K, 600 K, and 900 K.

These features enable the simultaneous optimization of the Seebeck coefficient and electrical conductivity, endowing n-type SrLiX with a higher PF.

3.4. Dimensionless figure of merit

Finally, to provide a comprehensive assessment of the thermoelectric performance of SrLiX (X = P, As), we analyzed the figure of merit ZT presented in Fig. 7, which serves as a key metric for evaluating the overall conversion efficiency of thermoelectric materials. The ZT values of both n-type SrLiP and SrLiAs increase with increasing temperature across the entire temperature range from 300 K to 900 K, indicating that higher temperatures favor thermoelectric performance in this system. Under the optimized conditions at 900 K, n-type SrLiP achieves a maximum ZT value of 0.73 at a carrier concentration of 1.89×10^{20} cm^{-3}, owing to its high PF and low

κ_L. The maximum ZT value of n-type SrLiAs is 0.48. At a given temperature, the maximum ZT values of n-type materials are higher than those of their p-type counterparts for both compounds, which is primarily attributed to the higher PF of the n-type materials. This work demonstrates that the substitution of As with the lighter anion P provides a viable pathway for designing high-performance ZrBeSi-type Zintl thermoelectrics.

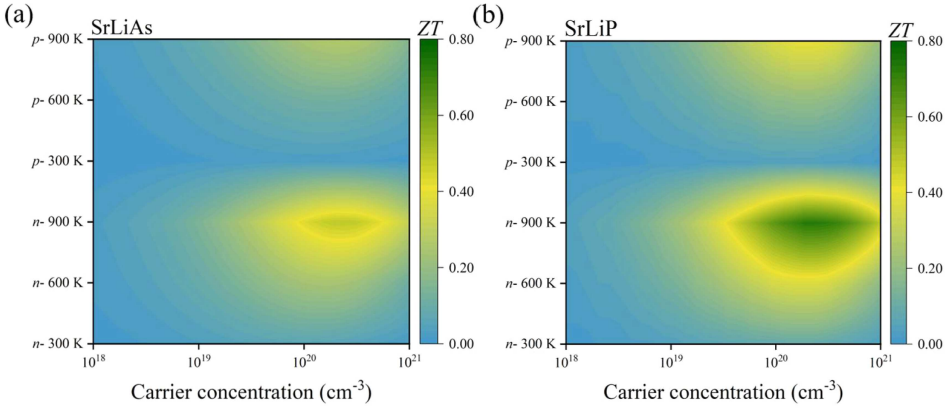

Fig. 7. The calculated thermoelectric figure of merit ZT for n-type and p-type SrLiAs and SrLiP at 300 K, 600 K, and 900 K.

4. Conclusion

In summary, using first-principles calculations combined with Boltzmann transport theory, we have demonstrated that the variation in anion species within the SrLiX (X = P, As) system enables an anomalous reduction in lattice thermal conductivity. Our findings reveal that the origin of this counterintuitive behavior can be traced to the expanded phonon bandwidth in SrLiP, which significantly enlarges the three-phonon scattering phase space and creates additional scattering channels. As a consequence, phonon scattering rates are substantially enhanced, leading to a pronounced suppression of lattice thermal conductivity. At 900 K, SrLiP achieves a low lattice thermal conductivity of 0.98 $\mathrm{W{\cdot}m^{-1}{\cdot}K^{-1}}$. On the electronic side, the CBM of SrLiX is characterized by multiple valley degeneracy accompanied by the coexistence of light and heavy bands. These unique band structures allow n-type SrLiX to maintain a high Seebeck coefficient while simultaneously delivering excellent electrical conductivity. Benefiting from this favorable combination, n-type SrLiP attains a PF of 1.33 $\mathrm{mW\cdot m^{-1}\cdot K^{-2}}$ at 900 K, while n-type SrLiAs reaches a PF of 1.14 $\mathrm{mW\cdot m^{-1}\cdot K^{-2}}$. Ultimately, the synergy between reduced κ_L and optimized PF enables n-type SrLiP to reach a ZT value of 0.73 at 900 K, higher than the 0.48 for n-type SrLiAs. This work paves the way for understanding the microscopic mechanism of the anomalously low κ_L.

Acknowledgments

This work was supported by the National Natural Science Foundation of China (Grant No. 52072188) and the Program for Science and Technology Innovation Team in Zhejiang, China (Grant No. 2021R01004). The authors acknowledge the Institute of High-Pressure Physics of Ningbo University for providing computational resources.

References

[1] Rowe D M 2005 *Thermoelectrics Handbook: Macro to Nano* (Boca Raton, FL: CRC Press)
[2] Li J, Han Z, Yu J, Zhuang H, Hu H, Su B, Li H, Jiang Y, Chen L, Liu W, Zheng Q and Li J 2023 *Nat. Commun.* **14** 7428
[3] Shi X, Li N, Li M and Chen Z 2025 *Chem. Rev.* **125** 7525
[4] Baskaran P and Rajasekar M 2024 *RSC Adv.* **14** 21706
[5] Snyder G J and Toberer E S 2008 *Nat. Mater.* **7** 105
[6] Zhao L, Chang C, Tan G and Kanatzidis M G 2016 *Energy Environ. Sci.* **9** 3044
[7] Yang C, Souchay D, Kneiß M, Bogner M, Wei H M, Lorenz M, Oeckler O, Benstetter G, Fu Y Q and Grundmann M 2017 *Nat. Commun.* **8** 16076
[8] Gao Y, Wang X, You C, Wang D, Gao N, Jia Q, Li Z, Tao Q and Zhu P 2025 *Chin. Phys. B* **34** 087201
[9] Pan Y, He B, Feng X, Li F, Chen D, Burkhardt U and Felser C 2025 *Nat. Mater.* **24** 76
[10] Su L, Wang D, Wang S, Qin B, Wang Y, Qin Y, Jin Y, Chang C and Zhao L 2022 *Science* **375** 1385
[11] Yazdani Kachoei M, Li S, Sun W, Allaei S M V and Di Marco I 2023 *Phys. Rev. Mater.* **7** 104602
[12] Li W, Ghosh S, Liu N and Poudel B 2024 *Joule* **8** 1274
[13] Anand S, Wood M, Xia Y, Wolverton C and Snyder G J 2019 *Joule* **3** 1226
[14] Zhao Z, Zhang X and Zhao L 2023 *Matter* **6** 3274
[15] Fiorentini V, Farris R, Argiolas E and Maccioni M B 2019 *Phys. Rev. Mater.* **3** 022401
[16] Cheng L, Li M, Zhang L and Wang H 2024 *Phys. Rev. B* **110** 155202
[17] Liu S, Bai S, Wen Y, Lou J, Jiang Y, Zhu Y, Liu D, Li Y, Shi H, Liu S, Wang L, Zheng J, Zhao Z, Qin Y, Liu Z, Gao X, Qin B, Chang C, Chang C and Zhao L D 2025 *Science* **387** 202
[18] Zhang W, Chen C, Yao H, Xue W, Li S, Bai F, Huang Y, Li X, Lin X, Cao F, Sui J, Wang S, Yu B, Wang Y, Liu X and Zhang Q 2020 *Chem. Mater.* **32** 6983
[19] Shi X, Song S, Gao G and Ren Z 2024 *Science* **384** 757
[20] Zhang P, Tang S, Bai S, Meng Y, Ai P, Zhang Z, Zhang Y, Bao Y and Wan D 2025 *Phys. Rev. B* **112** 024313
[21] Li F, Liu X, Chaudhary V, Xie R, Shen C, Wang H and Zhang H 2025 arXiv:2509.13204 [cond-mat.mtrl-sci]
[22] Zhu Y, Wang F, Li S, Shen C, Cai Y, Yan T, Zhang F, Wang Y, Zhan X, Xu K, Wang H, Zhang H, Wang Z and He J 2026 *Nat. Commun.* **17** 1180
[23] Cohn J L, Nolas G S, Fessatidis V, Metcalf T H and Slack G A 1999 *Phys. Rev. Lett.* **82** 779
[24] Kauzlarich S M, Brown S R and Snyder G J 2007 *Dalton Trans.* 2099

[25] Murtaza G, Ahad Khan A, Yaseen M, Laref A, Ullah N and ur Rahman I 2018 *Chin. Phys. B* **27** 047102

[26] Lin S, Yue J, Ren W, Shen C and Zhang H 2024 *J. Mater. Chem. A* **12** 19567

[27] Ren W, Yue J, Lin S, Shen C, Liu Y, Cui T and Zhang H 2026 *Front. Phys.* **21** 064203

[28] Seddik T, Uğur G, Khenata R, Uğur Ş, Soyalp F, Murtaza G, Rai D P, Bouhemadou A and Bin Omran S 2016 *Chin. Phys. B* **25** 107801

[29] Yuan M H, Le W K, Tan X J and Shuai J 2021 *Acta Phys. Sin.* **70** 207304 (in Chinese)

[30] Zhang C, Zhu J, Shen X, Shu M, Ren Q and Ma J 2025 *Acta Phys. Sin.* **74** 017301 (in Chinese)

[31] Zhou Z Z, Peng K L, Fu H X, Wu H, Wang G Y and Zhou X Y 2021 *Phys. Rev. Appl.* **16** 064034

[32] Feng Z, Fu Y, Yan Y, Zhang Y and Singh D J 2021 *Phys. Rev. B* **103** 224101

[33] Slack G A 1973 *J. Phys. Chem. Solids* **34** 321

[34] Hohenberg P and Kohn W 1964 *Phys. Rev.* **136** B864

[35] Kresse G and Hafner J 1993 *Phys. Rev. B* **48** 13115

[36] Perdew J P, Burke K and Wang Y 1996 *Phys. Rev. B* **54** 16533

[37] Pawar R and Sangolkar A A 2021 *Comput. Theor. Chem.* **1205** 113445

[38] Togo A 2023 *J. Phys. Soc. Jpn.* **92** 012001

[39] Li W, Lindsay L, Broido D A, Stewart D A and Mingo N 2012 *Phys. Rev. B* **86** 174307

[40] Li W, Carrete J, Katcho N A and Mingo N 2014 *Comput. Phys. Commun.* **185** 1747

[41] Ganose A M, Park J, Faghaninia A, Woods-Robinson R, Persson K A and Jain A 2021 *Nat. Commun.* **12** 2222

[42] Poncé S, Margine E R, Verdi C and Giustino F 2016 *Comput. Phys. Commun.* **209** 116

[43] Yue J, Zheng J, Li J, Shen X, Ren W, Liu Y and Cui T 2024 *Mater. Today Phys.* **46** 101517

[44] Jackson A J, Parrett B J, Willis J, Ganose A M, Leung W W, Liu Y, Williamson B A D, Kim T K, Hoesch M, Veiga L S I, Kalra R, Neu J, Schmuttenmaer C A, Lee T L, Regoutz A, Lee T C, Veal T D, Palgrave R G, Perry R and Scanlon D O 2022 *ACS Energy Lett.* **7** 3807

[45] Jiang B, Wang W, Liu S, Wang Y, Wang C, Chen Y, Xie L, Huang M and He J 2022 *Science* **377** 208

[46] Born M and Huang K 1996 *Dynamical Theory of Crystal Lattices* (Oxford: Oxford University Press)

[47] Mouhat F and Coudert F X 2014 *Phys. Rev. B* **90** 224104

[48] Cahill D G and Pohl R O 1988 *Annu. Rev. Phys. Chem.* **39** 93

[49] Kazemian S and Fanchini G 2025 *J. Phys.: Condens. Matter* **38** 153001

[50] Holland M G 1963 *Phys. Rev.* **132** 2461

[51] Yue J, Liu Y, Ren W, Lin S, Shen C, Singh H K, Cui T, Tadano T and Zhang H 2024 *Mater. Today Phys.* **41** 101340

[52] Shen J J, Fang T, Fu T Z, Xin J Z, Zhao X B and Zhu T J 2019 *J. Inorg. Mater.* **34** 260

[53] Singh D J and Parker D 2013 *J. Appl. Phys.* **114** 143703

[54] Cao W, Wang Z, Miao L, Shi J and Xiong R 2023 *Energy Environ. Mater.* **6** e12361

[55] Huang X, Li J, Ma H, Li C, Liu T, Duan B, Zhai P and Li G 2024 *Chin. Phys. Lett.* **41** 077102

[56] Zhao C, Cui S, Li T, Wu Y, Kong M, Bai W, Li K, Liu Y, Liu Z, Shang Z, Sun Z, Xiao C and Xie Y 2025 *Phys. Rev. Lett.* **134** 086401

[57] Shenoy U S and Bhat D K 2024 *J. Alloy Compd. Commun.* **1** 100001